International Journal of Nanomedicine

Dovepress
open access to scientific and medical research

Open Access Full Text Article

ORIGINAL RESEARCH

In-Situ Grown Nanocrystal TiO_2 on 2D Ti_3C_2 Nanosheets with Anti-Tumor Activity from Photo-Sonodynamic Treatment and Immunology

Hailing Yu[1,*], Yongquan Huang[2,*], Zhisheng Nong[3,*], Xi Lin[1], Kexin Tang[1], Zeyu Cai[1], Kaichen Huang[4], Ting Yu[1], Huimin Lan[1], Qianqian Zhang[1], Qiang Wang[5], Lei Yang[6], Jingchuan Zhu[7], Lili Wu[8], Hui Luo[1]

[1]Guangdong Provincial Engineering Research Center of Molecular Imaging, Guangdong-Hong Kong-Macao University Joint Laboratory of Interventional Medicine, The Fifth Affiliated Hospital, Sun Yat-Sen University, Zhuhai, Guangdong, People's Republic of China; [2]Department of Ultrasound, The Fifth Affiliated Hospital, Sun Yat-sen University, Zhuhai, Guangdong, People's Republic of China; [3]School of Materials Science and Engineering, Shenyang Aerospace University, Shenyang, Liaoning, People's Republic of China; [4]Department of Clinical laboratory, The Third People's Hospital of Zhuhai, Zhuhai, Guangdong, People's Republic of China; [5]The Green Aerotechnics Research Institute of Chongqing Jiaotong University, Chongqing, People's Republic of China; [6]Center for Composite Materials and Structures, Harbin Institute of Technology, Harbin, Heilongjiang, People's Republic of China; [7]School of Materials Science and Engineering, Harbin Institute of Technology, Harbin, Heilongjiang, People's Republic of China; [8]Key Laboratory for Photonic and Electronic Bandgap Materials, Ministry of Education, School of Physics and Electronic Engineering, Harbin Normal University, Harbin, Heilongjiang, People's Republic of China

*These authors contributed equally to this work

Correspondence: Hui Luo; Lili Wu, Email luoh53@mail.sysu.edu.cn; wll790107@hotmail.com

Introduction: Traditional cancer treatment strategies often have severe toxic side effects and poor therapeutic efficacy. To address the long-standing problems related to overcoming the complexity of tumors, we develop a novel nanozyme based on the in situ oxidation of 2D Ti_3C_2 structure to perform simultaneous phototherapy and sonodynamic therapy on tumors. Ti_3C_2 nanozymes exhibit multi-enzyme activity, including intrinsic peroxidase (POD) activities, which can react with H_2O_2 in the tumor microenvironment. This new material can construct Ti_3C_2/TiO_2 heterostructures in vivo.

Methods: Photothermal (PTT), sonodynamic (SDT) effects, and photoacoustic (PA) image-guided synergy therapy can be achieved. Finally, anticancer immune responses occur with this nanozyme. In vivo experiments revealed that the Ti_3C_2/TiO_2 heterostructure inhibited tumor growth.

Results: Complementarily, our results showed that the Ti_3C_2/TiO_2 heterostructure enhanced the immunogenic activity of tumors by recruiting cytotoxic T cells, thereby enhancing the tumor ablation effect. Mechanistic studies consistently indicated that Reactive Oxygen Species (ROS) regulates apoptosis of HCC cells by modulating NRF2/OSGIN1 signaling both in vitro and in vivo. As a result, Ti_3C_2 nanozyme effectively inhibited tumor through its synergistic ability to modulate ROS and enhance immune infiltration of cytotoxic T cells in the tumor microenvironment.

Discussion: These findings open up new avenues for enhancing 2D Ti_3C_2 nanosheets and suggest a new way to develop more effective sonosensitizers for the treatment of cancer.

Keywords: nanozyme, sonodynamic therapy, Ti_3C_2/TiO_2, ROS

Introduction

Hepatocellular carcinoma (HCC) was a dominant form of primary liver cancer and was the fifth most common malignant cancer in the world.[1] Recent advances in nanotechnology have significantly accelerated the development of novel therapies for HCC, but more effective treatment for patients remains an unmet clinical need.[2,3] Numerous studies show that photothermal therapy (PTT) effectively treats malignant cancers.[4–6] However, PTT has been limited in clinical application due to its intrinsic drawbacks, including phototoxicity and low penetration depth into tumor

Received: 29 December 2023
Accepted: 6 July 2024
Published: 6 August 2024

regions.[7,8] In addition, PTT cannot ablate the entire solid tumor or large tumors due to its penetration depth. The residual tumor after PTT might become activated and lead to tumor metastasis and recurrence.[9] Thus, there is still a great unmet need to exploit novel therapies or synergistic methods to overcome these limitations.

In recent years, nanocatalytic therapies based on the generation of ROS in the tumor microenvironment (TME) have attracted much attention.[10] Nanozyme-mediated catalytic tumor therapy has been widely used with the advantages of high stability, low cost, adjustable catalytic activity, and in situ catalytic reaction in vivo. Our previous study showed that nanomaterials with catalytic activity can specifically induce ROS production in tumor cells, thereby inducing mitochondrial damage.[11] Among them, nanomaterials with peroxidase (POD)-like activity, which kills cancer cells by generating reactive hydroxyl radicals (·OH) upon reaction with H_2O_2, have attracted widespread attention. However, due to the generally low H_2O_2 concentration in the tumor microenvironment, as well as the heterogeneity of tumors, low catalytic activity limited therapeutic efficiency. Therefore, there is an urgent need for more efficient nanozymes with multiple effects that can effectively accumulate and release ROS to enhance tumor therapeutic effects.

MXene is a class of new 2D materials with excellent physical and chemical properties that have a wide range of promising applications in energy storage, wastewater treatment, and hydrogen storage.[12] Ti_3C_2 is the typical representative of MXene, due to its good absorption in the NIR I and NIR II regions and excellent photothermal properties.[13] The exfoliated Ti_3C_2 MXene is mildly oxidized with H_2O_2 to produce titanium oxide nanoclusters anchored to the substrate. TiO_2 is a representative of inorganic sonosensitizers for SDT. SDT is a new non-invasive and high tissue penetration therapy that uses ultrasound to simulate sonosensitizer to generate ROS, induce tumor cell death, and achieve therapeutic purposes.[14,15] Based on the deep tissue penetration ability of ultrasound, SDT can realize the treatment of deeper tumors and has broad prospects for preclinical studies.[16,17] Current sonosensitizers are divided into two types, inorganic and organic sonosensitizers.[18,19] The therapeutic efficacy of organic sonosensitizers, including porphyrin and its derivatives, is limited by poor bioavailability, unsatisfactory efficacy, and off-target toxicity. Compared to organic sonosensitizers, TiO_2, as an important member of inorganic sonosensitizers, has excellent physiochemical stability and biocompatibility.[20,21] Although the SDT performance of TiO_2 nanomaterials can be improved by combining TiO_2 nanomaterials with Pt, Au, and Ag to form heterostructures or oxygen defect sites in TiO_2 nanomaterials, it is still necessary to improve the effect of sonosensitizers and enhance synergistic therapy.[22–25] Since the surface of Ti_3C_2 MXenes nanosheet very easily undergoes oxidation reaction, titanium atoms on Ti_3C_2 can be used as nucleation sites to generate TiO_2, thus forming Ti_3C_2/TiO_2 heterostructure. Ti_3C_2 is an ideal nanoplatform for combining PDT and SDT to enhance the efficacy of SDT and exhibits excellent photoacoustic (PA) imaging properties.[26]

In this study, we fabricated Ti_3C_2 Mxene with catalytic effect by chemical etching, and Ti_3C_2 exhibits multi-enzyme activity, including intrinsic peroxidase (POD) activities, which can react with H_2O_2 in the TME and are accompanied by ROS generation. The surface defects in Ti_3C_2 are gently oxidized in situ by H_2O_2 in the TME to construct a Ti_3C_2/TiO_2 heterostructure, integrating photothermal and sonodynamic effects to achieve image-guided tumor therapy and induce multiple anticancer immune responses. It is demonstrated that Ti_3C_2/TiO_2 heterostructure is an excellent sonodynamic and photothermal sensitizer for tumor therapy, showing excellent photothermal/sonodynamic properties at NIR broadband and immunomodulatory function both in vivo and in vitro, as shown in Figure 1. Notably, we found that the combination of sonodynamic and photothermal therapies based on Ti_3C_2/TiO_2 induced the TME from "cold" to "hot" in HCC mouse models. Our studies accelerate the application of Ti_3C_2 nanozyme-mediated sonodynamic and photothermal synergistic therapy for HCC treatment by activating the immune tumor microenvironment.

Materials and Methods

Preparation of Ti_3C_2 and Ti_3C_2/TiO_2

Lithium fluoride was slowly poured into a hydrochloric acid solution and stirred by a magnetic stirrer for 10 min. Ti_3C_2 was prepared by etching Ti_3AlC_2 powder by mixing a solution of lithium fluoride and hydrochloric acid for 24 h. Then the solution was centrifuged at 8000 rpm for 10 min, and the precipitates were washed with lithium fluoride, hydrochloric acid, and water in sequence until the pH reached 7.4. The Ti_3C_2 solution was lyophilized and freeze-dried for further experiments. 0.1 mL H_2O_2 (10 mM) was added to the Ti_3C_2 solution (10 mg/mL) and allowed to react for 24 h, and then Ti_3C_2/TiO_2 was obtained.

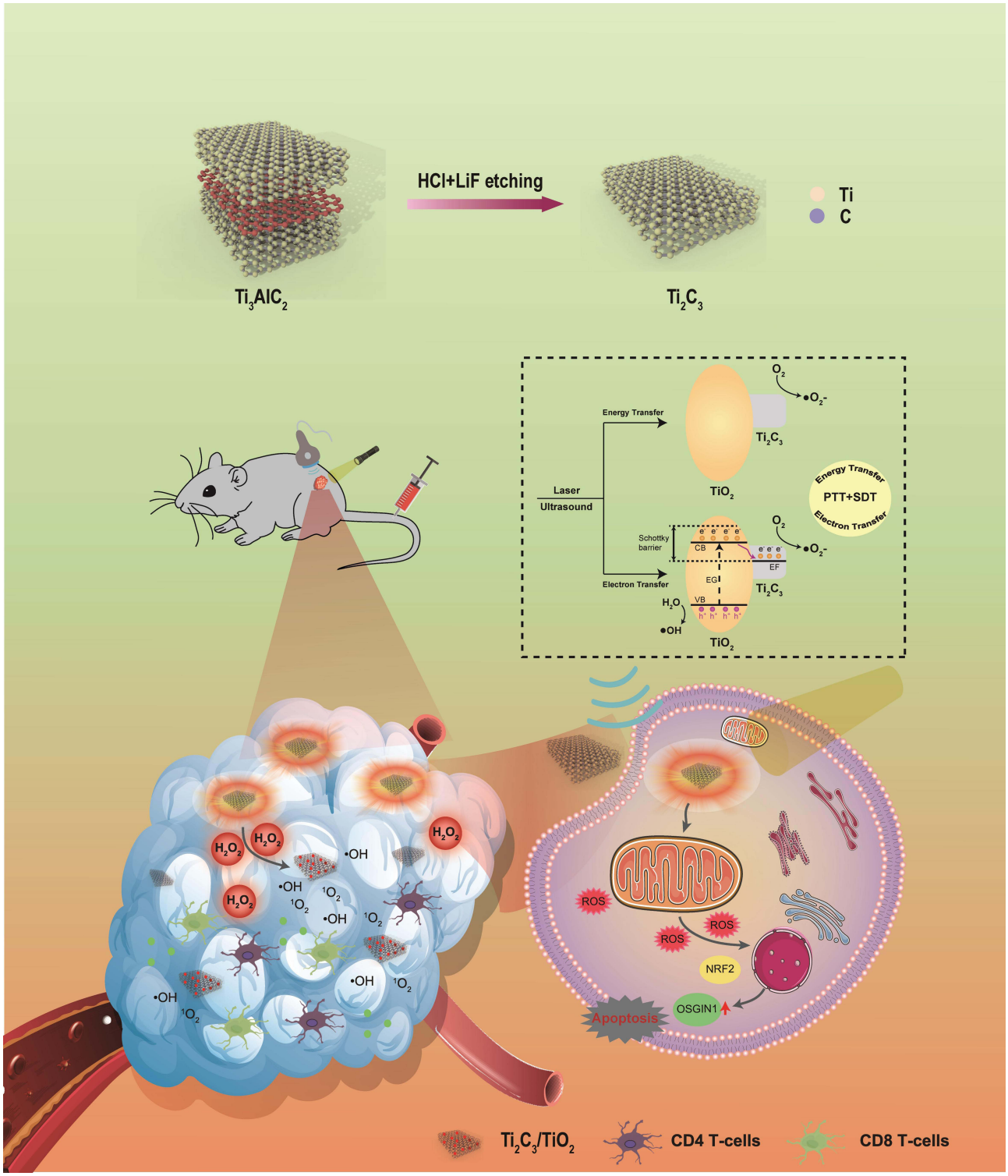

Figure 1 The schematic diagram of in-situ grown nanocrystal TiO_2 on 2D Ti_3C_2 nanosheets with photo-sonodynamic activity enhanced tumor ablation by immunotherapy. Unraveling the mechanisms underlying SDT-regulated ROS via OSGIN1 signaling was conducive to gaining a deeper understanding of the role of oxidative stress in HCC therapies and accelerating the clinical transformation of SDT.

Materials

Dulbecco's modified Eagle's medium Dulbecco (DMEM), fetal bovine serum, penicillin-streptomycin, and trypsin-EDTA were purchased from ThermoFisher Scientific (USA). Calcein-AM/propidium iodide (PI) kit and dichlorofluorescin diacetate

(DCFH-DA) probe were purchased from Beyotime Biotechnology (China). The cell counting kit (CCK-8) was purchased from Dojindo Laboratories (Japan).

DFT Calculation

Ti_3C_2 and the absorption of H_2O_2 were calculated from first principles using density functional theory (DFT) in the Cambridge Serial Total Energy Package (CASTEP) code. In these calculations, the ultra-soft pseudo-potential was used to describe the interaction between the electron and the ion, and the electron exchange-correlation function was applied by generalized gradient approximation (GGA) of Perdew Burke Ernzerhof (PBE). The cut-off energies of 380 eV were used in the calculation. The appropriate grids of the k-point mesh were selected on the basis of the Monkhorst-Pack scheme. The self-consistent first-principles calculations converged when the maximum force on the atom, the maximum displacement between cycles, the maximum stress, and the total energy changes at each atom were less than 0.01 eV/Å, 5.0×10^{-4}Å, 0.02 GPa, and 5.0×10^{-6} eV/atom, respectively.

Cell Culture

Human hepatocellular carcinoma cells Hep3B, Bel-7402, SK-Hep-1, and human kidney cells (HEK 293T) were purchased from Jennio Biotech Co., Ltd (Guangzhou, China). All cells were cultured in Dulbecco's modified Eagle's medium (DMEM) (for Hep3B cells) or RPMI 1640 medium (for SK-Hep-1 and Bel 7402 cells) supplemented with 10% fetal bovine serum (FBS, Gibco, USA) and 1% penicillin-streptomycin (PS, Gibco, USA). They were maintained in an incubator under 5% CO_2 at a constant temperature of 37°C. For sphere-forming assays, Hep3B and SK-Hep-1 cells were cultured in a 100 mm Ultra-Low Attachment Culture Dish (Corning, USA) to form tumor cell spheroids (50–100 μm).

In vitro Cytotoxicity of Ti_3C_2

The cytotoxicity of Ti_3C_2 at different concentrations was evaluated using the CCK-8 assay. Cells were plated in 96-well plates (5×10^3 cells per well) for 24 h and then incubated with 20 μg/mL Ti_3C_2 for 12 h. Then, cells were subjected to different treatments as follows: (1) Cells were exposed to ultrasound at 1 W/cm^2 for different times (0, 1, 2, 3, 4 minutes). (2) Cells were exposed to ultrasound at different power levels (0, 0.5, 0.75, 1, 1.25 W/cm^2) for 3 minutes. (3) Cells were exposed to laser at 1 W/cm^2 for different periods (0, 1, 2, 3 minutes). (4) Cells were exposed to different laser powers (0, 0.5, 1, 1.5 W/cm^2) for 2 min. (5) Cells were exposed to ultrasound (1 W/cm^2, 3 min) and laser (1 W/cm^2, 2 min). The cells were then cultured for a further 12 or 18 hours. Finally, the CCK-8 test was performed to measure cell viability, and absorbance at 450 nm was measured using a multimode microplate reader (PerkinElmer EnVision 2105, USA). Calcein-AM/PI staining experiments were also performed to evaluate the in vitro therapeutic efficacy of Ti_3C_2.

Detection of ROS

The extracellular ROS generated by laser and ultrasound stimulation was dynamically detected by DCFH-DA, which could be oxidized by ROS to generate the fluorescence of DCF (Beyotime, China). Hep3B cells (2×10^5 per well) were cultured in 6-well plates with DMEM at 37 °C for 24 h. After co-incubation with 20 μg/mL Ti_3C_2 for 8 h, the cells were treated with 1 W/cm^2 808 nm laser for 5 min; 1 W/cm^2 ultrasound stimulation for 3 min, and both laser and ultrasound irradiation. The cells were treated with different ultrasound power densities (0, 0.5, 1, 1.25 W/cm^2). The treated cells were cultured in Incucyte (ESSEN Bioscience, Incucyte S3, USA) for 48 h and dynamically detected by the fluorescence intensity of DCFH.

Hep3B and SK-Hep-1 mammospheres (50–100 μm) were incubated with 20 μg/mL Ti_3C_2 for 8 h. The mammospheres were treated with 1 W/cm^2 808 nm laser for 5 min, 1 W /cm^2 ultrasound for 3 min, and both laser and ultrasound. The spheroids were treated with different ultrasound power densities (0, 0.5, 1, 1.25 W/cm^2). The treated mammospheres were incubated with DCFH-DA for 12 h, washed with PBS and centrifuged at 800 rpm for 3 min, then resuspended in PBS for detection by CLSM including Z-stack imaging (Carl Zeiss LSCM 880, Germany).

In vitro Photothermal Effect of Ti_3C_2

The in vitro photothermal effect of Ti_3C_2/TiO_2 was measured separately under 808 nm, or 1064 nm laser irradiation (1 W/cm^2) for 10 min at different concentrations (25, 50, 100, and 200 μg/mL). The photothermal stability of Ti_3C_2/TiO_2 was tested by measuring the periodic heating under 808, or 1064 nm laser irradiation (1 W/cm^2) for 10 min and the cooling process of Ti_3C_2/TiO_2 for 5 cycles. Hep3B, Bel-7402, and SK-Hep-1 were cultured in 10 cm dishes with DMEM at 37 °C and incubated with 40 μg/mL Ti_3C_2/TiO_2 for 8 h, then washed with PBS and centrifuged at 800 rpm for 3 min. The cell mass was collected and measured under 808, or 1064 nm laser irradiation (1 W/cm^2) for 10 min. All infrared thermographs were taken using a Fluke thermal imager (Fluke, USA), and the temperature was recorded.

Cellular Uptake of Ti_3C_2 in vitro

Hep3B cells were seeded into the 6-well cell culture plate at a density of 1×10^5 cells per well. Hep3B cells were then incubated with 5-FAM-labelled Ti_3C_2 (20 μg/mL) for different time intervals (0, 2, 4, 6, 8, 12 h). Cells were harvested and detected by flow cytometry using the B525-FITC channel. Hep3B cells were seeded into the cover glass bottom dish at a density of 10^5 cells per well. Hep3B cells were incubated with Ti_3C_2 (20 μg/mL) labeled with Cy-5 for different time intervals (0, 2, 4, 6, 8, 12 h). The cells were then detected and photographed using laser confocal scanning microscopy.

Photoacoustic Imaging

Ti_3C_2 dispersed in PBS solution and photoacoustic images of Ti_3C_2 at different concentrations (0, 25, 50, 150, 200 μg/mL) in vitro were photographed using the Vevo FUJIFILM VisualSonics system. Ti_3C_2 solution was injected intravenously into the tumor-bearing mouse and photographed at different time intervals (0, 2, 4, 6, 8, 10, 12, 24 h).

Western Blot

Western blot assays were carried out as previously described. Briefly, cells were treated as indicated. Total cellular lysates were prepared and followed to SDS-PAGE. Gels were then electro transferred to PVDF membranes and blotted against the primary antibodies after being blocked with 5% milk solution. Primary antibodies against GAPDH, Cleaved caspase 3, Cleaved PARP, and P53 were purchased from Cell Signaling Technology (USA). Antibodies against NRF2 were obtained from Abcam (UK), and OSGIN1 was purchased from Proteintech (USA). HRP-conjugated antibodies were then incubated with the membranes and subjected to ECL analysis. Chemiluminescence results were captured by iBright FL1500 (Invitrogen, Thermofisher Scientific, USA).

RNA-Seq Analysis and Quantitative PCR

Briefly, cells were lysed in Trizol solution, and mRNA was obtained by Ribobio Company (Guangzhou, China). Transcriptome analyses were performed and results were analyzed by GraphPad software. Quantitative PCR experiments were conducted by RT-qPCR mix (Takara, Japan). Results from three independent experiments were statistically analyzed and graphed.

Immunohistochemistry (IHC) Assays

Tissue slides were cropped into 5 μm slices and subjected to dewaxing, H&E and IHC analysis were carried out as previously described. Briefly, slices were incubated with antibodies against CD4, CD8, TNF-α, and IFN-γ (Bioss, Beijing, China). Subsequently, they were subjected to DAB staining and scanned by 3D Histech. Representative pictures were shown from each treated group.

Immunofluorescence Staining

Cells were cultured in sterilized over slides plated in 6-well plates and treated as indicated. After the treatment cover slides were fixed with 4% paraformaldehyde and permeabilized by Triton-X100. Then, cells were stained with primary antibodies, followed by Alexafluo-488nm or 596 nm conjugated secondary antibodies. DAPI was used as counterstaining

to visualize nucleus. Cells were then transferred to slides and observed under confocal laser scanning microscopes. For tissues, slides from OCT-embedded tumor tissues were prepared freshly after being excised freshly from animal models and deposited at −80 °C. Just before use, cells were rewarmed to temperature. Slides were rinsed with PBS solution and stained with the antibodies as described above.

Animal Studies

H22 cells were inoculated subcutaneously into Balb/c mice. Two weeks after inoculation, when tumors grow to palpable size. Mice were randomly divided into five groups and treated with PBS, Ti_3C_2, Ti_3C_2+ultrasound, Ti_3C_2+laser, Ti_3C_2 +ultrasound+laser. For the bilateral subcutaneous model, H22 cells were inoculated on two sides on the back, proximal side of one group received Ti_3C_2 +ultrasound+laser treatment, while the distal tumors were not. Body weight and tumor size were recorded every four days just before each treatment. After six treatment sessions, blood was collected and the mice were anesthetized. Organs were harvested, followed by ICP testing or fixed in paraformaldehyde. Tumors were weighed and measured. Photographs were taken of each group to compare the size of each group. All tumors were fixed for further immunohistochemistry or H&E analysis. All animal studies were conducted in accordance with the National Animal Welfare Guidelines (GB/T 35892–2018) and approved by the Animal Ethics Committee of the Fifth Affiliated Hospital of Sun Yat-sen University (Approval No. 00153).

Statistical Analysis

All experiments were performed at least three times. Representative images were selected to be shown in the figures. All figures were plotted and statistically analyzed using GraphPad prism 8.0 software. Student's *t*-test or two-way ANOVA was used to compare two or more groups. $p<0.05$ was considered statistically significant.

Results and Discussion

Synthesis and Characterization of Ti_3C_2 and Ti_3C_2/TiO_2

Ti_3C_2 was synthesized by a chemical exfoliation strategy according to the previous report.[27] The Ti_3AlC_2 power was etched by LiF and HCl solutions for removing the Al layer, and the Ti_3C_2 layer was obtained after centrifugation. TEM image of Ti_3C_2 layer has been shown in Figure 2A, and the AFM image of Ti_3C_2 layer revealed a 2D structure (Figure 2B). The XRD result showed that the nanostructure consists of Ti_3C_2, as shown in Figure 2C. Defects in Ti_3C_2 nanosheets can react with H_2O_2 to form the two-dimensional heterogeneous Ti_3C_2/TiO_2 structure in situ. The Ti_3C_2/TiO_2 heterostructures were prepared by the oxidation reaction of Ti_3C_2 and transmission electron microscopy (TEM) revealed an ultrathin layer structure of Ti_3C_2/TiO_2, as shown in Figure 2D. Ti_3C_2/TiO_2 has a fusiform shape and the size of the obtained nanostructure is 100–200 nm. There are some wrinkles on the nano-layer. The HRTEM images showed that the TiO_2 was randomly decorated on the Ti_3C_2 layers (Figure 2E). The XRD pattern in Figure 2F confirmed that the composite structure was composed of Ti_3C_2 and TiO_2. ESR measurements showed that Ti_3C_2 can convert H_2O_2 to ·OH and $^1O_2$, and ultrasound enhances the generation of ·OH and $^1O_2$. (Figure 2G and H). The Zeta potential is shown in Figure S4.

Figure 2I shows XPS spectra of Ti_3C_2 and Ti_3C_2/TiO_2 heterostructures. The full XPS spectra show O 1s, Ti 2p, and C1s peaks at 530.2, 456.2, and 283.5 eV for both samples. The Al 1s peak appears negligibly small, indicating good removal of Al layers during the etching process. The O 1s peak intensity of Ti_3C_2/TiO_2 heterostructure is much stronger than that of $Ti_3C_2T_x$ MXene, which means that there is a significant amount of oxide in the heterostructure. Interestingly, the F 1s peak is clearly found at 683.4 eV for $Ti_3C_2T_x$, but it is drastically reduced for Ti_3C_2/TiO_2, suggesting that most of the F functional groups on the original MXene disappear during the transformation. Focused XPS spectra of Ti 2p and C 1s are shown in Figure 2J and K. The Ti 2p3/2 components centered at 455.4, 456.3, 457.5, and 459.2 eV are attributed to Ti-C bonds, Ti-X from titanium oxycarbides or substoichiometric TiC_x ($x < 1$), Ti ions with reduced charge state (Ti_xO_y) and Ti^{4+} ions (TiO_2), respectively.[28] After oxidation with H_2O_2, the relative percentage of Ti^{4+} ions (TiO_2) increases from 6.14% to 60.60%, and the relative percentage of Ti-C bonds shows a remarkable decrease from 31.87% (for Ti_3C_2) to 14.91% of (for Ti_3C_2/TiO_2), indicating that a part of Ti_3C_2 was converted to TiO_2 by oxidation with H_2O_2. The C 1s XPS spectrum of Ti_3C_2 shows five

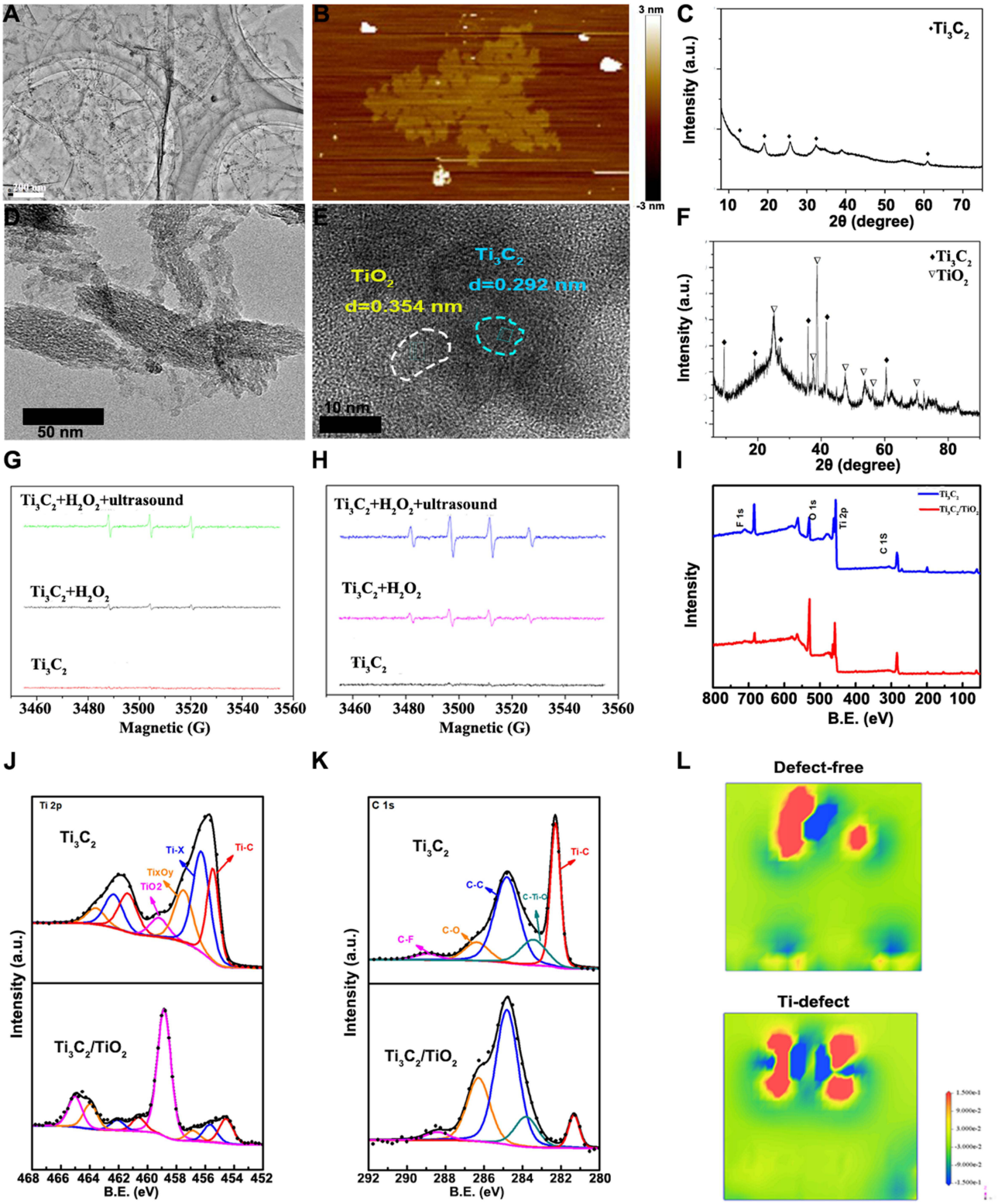

Figure 2 Characterization of Ti_3C_2 and Ti_3C_2/TiO_2. (**A**) TEM image of Ti_3C_2; (**B**) AFM image of Ti_3C_2; (**C**) XRD result of Ti_3C_2; (**D**) TEM image of Ti_3C_2/TiO_2; (**E**) The HRTEM image of Ti_3C_2/TiO_2; (**F**) XRD pattern of Ti_3C_2/TiO_2; ESR spectrum of Ti_3C_2 under different conditions, (**G**) the trapping agent is DMPO and (**H**) trapping agent is TEMP; (**I**) XPS of Ti_3C_2 and Ti_3C_2/TiO_2; (**J**) Ti 2p, (**K**) C 1s spectra of Ti_3C_2 and Ti_3C_2/TiO_2; (**L**) Top view of adsorption behaviors between $Ti_3C_2T_x$(T_x=-O) and H_2O_2 molecule. The electron density difference of the $Ti_3C_2T_x$ (T_x=-O) at the defect-free system and Ti–defected system. Red and blue colors indicate electron accumulation and depletion, respectively. (**I**–**K** are graphed by origin 9.0).

obvious peaks at 282.3, 283.4, 284.8, 286.4, and 288.9 eV, corresponding to Ti-C, C-Ti-O, C-C, C-O and C-F bonds, respectively.[29]

The oxidation process by H_2O_2 in situ was hypothesized by DFT calculations. First, we constructed the Ti_3C_2 monolayer structures with and without defects, as illustrated in Figure S1. We optimized the geometries of the $Ti_3C_2T_x$ (T_x=-O) monolayer structure. The DFT calculated the atomic electron density difference maps, which are displayed in Figure 2L. The blue area indicates a decrease in electron density, while the red area indicates an increase. Figure S1 shows the atomic electron density difference maps of cross-sections that include H_2O_2 and Ti_3C_2 atoms. Figure 2L presents an enlarged view of the selected cross-sections, displaying the electron density difference. The coordinates on the right indicate the electron gain and loss for each Ti_3C_2 atom before and after the H_2O_2 adsorption. "+" and "-" signs indicate electron gain and loss, respectively. The electron density difference map of the Ti_3C_2 with titanium vacancies indicates an enlarged electron gain and loss region, revealing increased bonding between atoms. Additionally, the presence of Ti defects enhances the electron gain ability of H_2O_2, indicating stronger binding interactions between H_2O_2 and the surface of Ti_3C_2. The DFT calculations showed that Ti vacancies in Ti_3C_2 were the primary reactive site for the oxidation of Ti_3C_2 to form Ti_3C_2/TiO_2 heterostructures.

Photothermal Effect of Ti_3C_2 Nanoparticles

To investigate the photothermal conversion of nanoparticles, we applied a gradient concentration of Ti_3C_2 in a solution. We then examined its photothermal effect after irradiation with a near-infrared imager. The results demonstrate that varying concentrations of Ti_3C_2 caused an increase in temperature in the solution under both laser irradiations. The temperature of the Ti_3C_2 solution increased with 808 nm or 1064 nm laser irradiation (1 W/cm^2), resulting in a rise from 40.8 °C to 53.9 °C and from 43.3 °C to 81.2 °C, respectively (Figure 3A–C). When the laser power increased from 0.5 W to 1.5 W, the Ti_3C_2 solution escalated from 40.6 °C to 64.8 °C (200 ppm, 808 nm, Figure 3B). Similarly, the temperature of Ti_3C_2 (200 ppm) increased from 45.5 °C to 84.0 °C under 1064 nm irradiation (Figure 3D). The photothermal stability was successfully demonstrated by subjecting it to either an 808 nm or 1064 nm laser (1 W/cm^2) for 5 minutes and cooling it to room temperature for five cycles. No degradation was observed after 5 heating and cooling cycles, even under continuous laser irradiation (Figure 3E and F). These results indicate that Ti_3C_2 possesses superior photothermal stability and has the potential to be used as a photosensitizer in the NIR region. Based on the results obtained from the Ti_3C_2 solution, we incubated Hep3B cells with Ti_3C_2. We consistently observed a gradual increase in temperature after NIR light irradiation at both 808 and 1064 nm. PBS-treated cells did not display any significant temperature increase. This supports the conclusion that Ti_3C_2 induced a specific temperature increase in Hep3B cells, as shown in Figure 3G and H. To determine the photothermal effect of Ti_3C_2 in vivo, we established a subcutaneous xenograft model and analyzed the photothermal conversion of Ti_3C_2/TiO_2. Ti_3C_2 was injected into the tail vein, and we used an infrared camera to detect the temperature increase induced by 808 nm or 1064 nm laser in the tumors. This experiment provides further insight into the photothermal properties of Ti_3C_2/TiO_2 in vivo. As shown in Figure 3I and J, Ti_3C_2/TiO_2 groups irradiated with 2 W/cm^2 of 808 nm or 1064 nm irradiance recorded a significant temperature increase to 57.7 °C and 86.7 °C, respectively. Taken together, these findings demonstrate that Ti_3C_2/TiO_2 exhibits exceptional photothermal conversion efficiency and stability, rendering it a promising candidate for tumor eradication.

Cellular Uptake of Ti_3C_2

Since the uptake of nanodrugs into tumor cells is necessary for their anti-tumor effect, we analyzed the uptake of our nanoparticles in HCC cells using confocal laser scanning microscopy and flow cytometry assays. Figures 4A and S5 display increased Cy5 signals under microscopy, indicating the gradual uptake of Ti_3C_2 by HCC cells with extended treatment. The flow cytometry results quantified that the maximum uptake of Ti_3C_2 occurred at 12 hours (Figure 4B and C). This study demonstrated that Ti_3C_2 was internalized by HCC cells in a time-dependent manner, indicating its potential for future therapeutic applications. The depth of nanodrug penetration into tumor spheres may ensure adequate drug delivery into tumor tissues. To verify this, we incubated Hep3B tumor mammospheres with 5'FAM-labeled Ti_3C_2 and assessed its penetration using the Z-stack mode of confocal laser scanning microscopy. As depicted in Figure 4D,

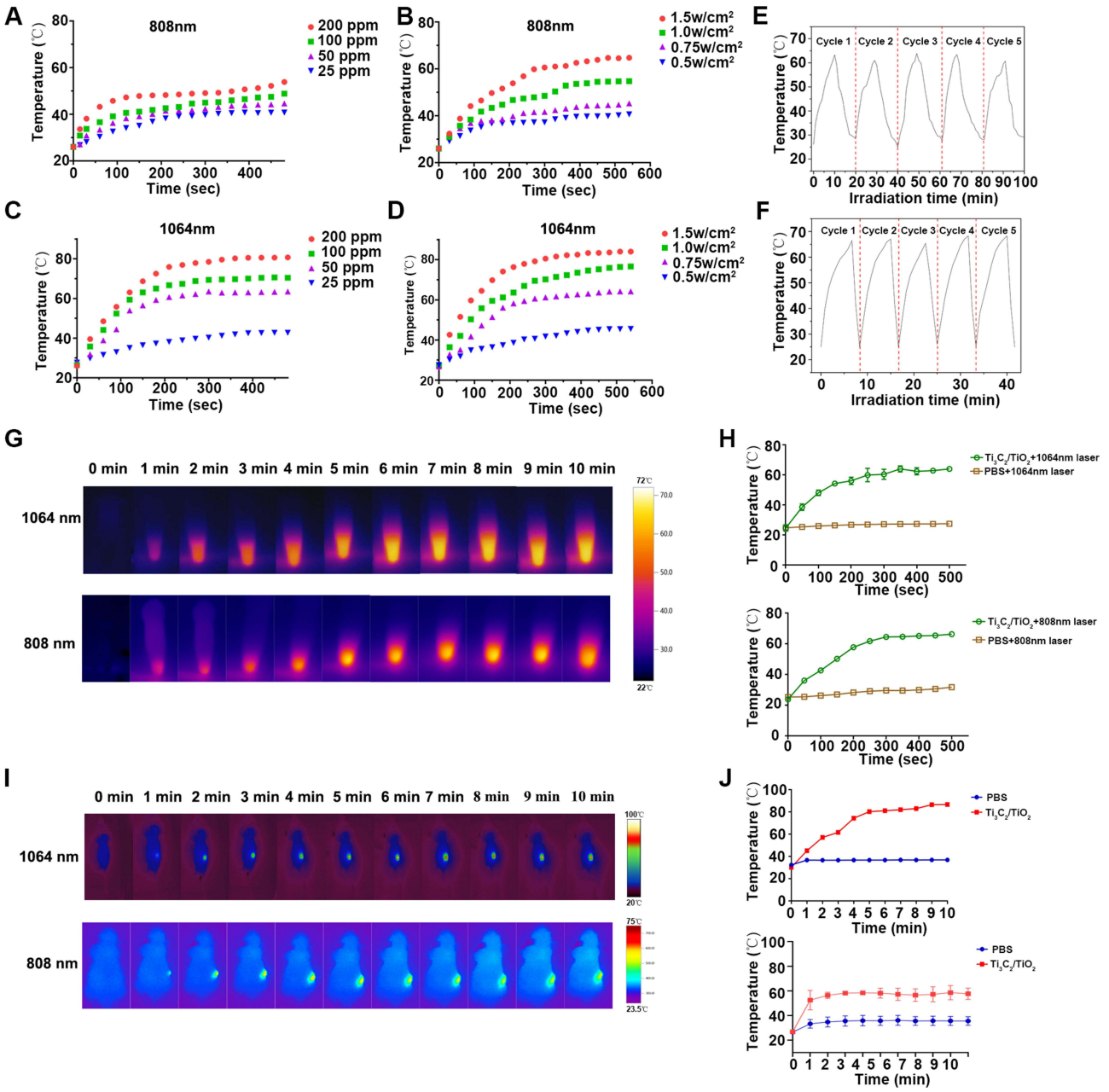

Figure 3 Photothermal effect of Ti_3C_2 in vitro and in vivo. (**A**) The photothermal conversion of various Ti_3C_2 concentrations under 808 nm laser irradiation (1 W cm^{-2}); (**B**) The photothermal conversion of Ti_3C_2 concentrations under various laser irradiation power (100 ppm, 808 nm); (**C**) The photothermal conversion of various Ti_3C_2 concentrations under 1064 nm laser irradiation (1 W cm^{-2}); (**D**) The photothermal conversion of Ti_3C_2 concentrations under various laser irradiation power (100 ppm, 1064 nm); (**E**) Photothermal stability study of Ti_3C_2 during five circles of heating-cooling processes. (1 W cm^{-2}, 200 ppm, 808 nm); (**F**) Photothermal stability of Ti_3C_2 during five circles of heating-cooling processes. (1 W cm^{-2}, 200 ppm, 1064 nm); (**G**) The photothermal conversion of Ti_3C_2 in vivo under 1064 nm or 808 nm laser irradiation; (**H**) The quantification of photothermal conversion of Ti_3C_2 under 1064 nm or 808 nm laser irradiation in vivo; (**I**) The photothermal conversion of Ti_3C_2 under 1064 or 808 nm laser irradiation in vivo. (**J**) The quantification of photothermal conversion of Ti_3C_2 under 1064 or 808 nm laser irradiation in vivo.

Ti_3C_2/TiO_2 exhibits a superior penetration depth within the tumor mammospheres in comparison to 5-FAM, which only penetrates the surface. This observation validates Ti_3C_2 capability to penetrate the mammospheres significantly. The combination of high uptake and deep penetration contributes to the accumulation of Ti_3C_2/TiO_2 in the core of the tumor and the therapeutic efficacy of Ti_3C_2/TiO_2.

The excellent photoacoustic (PA) property of Ti_3C_2 is due to its NIR abundance and good photothermal conversion ability. The accumulation of Ti_3C_2/TiO_2 in the tumor section was confirmed through photoacoustic imaging. Ti_3C_2/TiO_2 at different concentrations was detected by PA tomography in Figure 4E. As the Ti_3C_2/TiO_2 concentration was increased

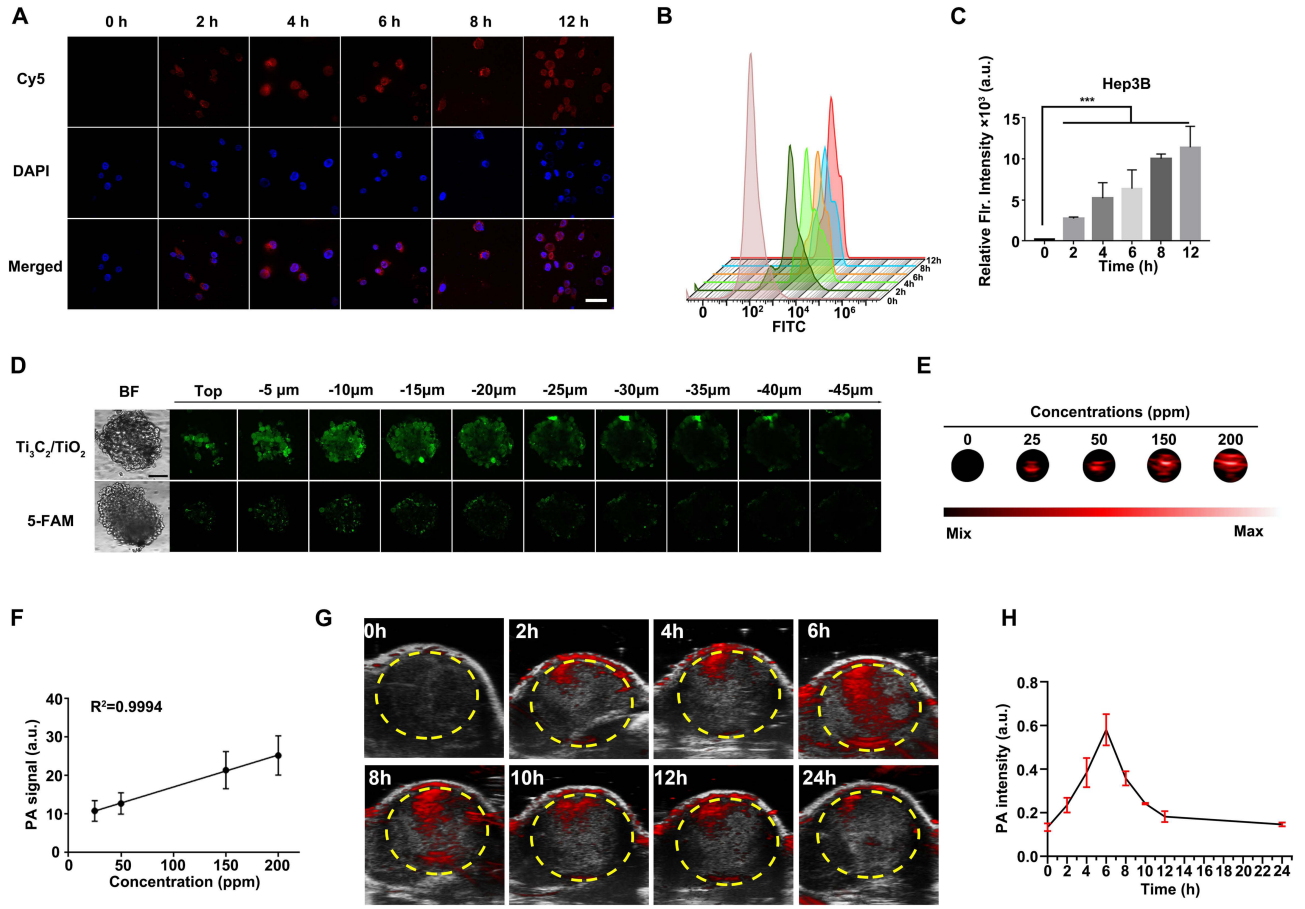

Figure 4 Uptake and photoacoustic effect of Ti_3C_2 in HCC cells. (**A**) The uptake of Hep3B cells incubated with Ti_3C_2 at various time intervals (20 ppm), red signals indicate Cy5, nuclei were counterstained with DAPI (blue); (**B**) The uptake of Ti_3C_2 was evaluated by flow cytometry after incubation with Cy5-labelled-Ti_3C_2 for indicated periods; (**C**) The quantity of the uptake of Hep3B cells incubated with Ti_3C_2, **** indicates $p<0.0001$; (**D**) The Z-stack images of Hep3B mammospheres incubated with Ti_3C_2 or 5-FAM by CLSM. Scale bar: 200μm; (**E**) PA images at various concentrations of Ti_3C_2/TiO_2; (**F**) The relationship between PA signal intensities and concentrations of Ti_3C_2/TiO_2; (**G**) PA signal intensities of the tumor after intravenous injection of Ti_3C_2/TiO_2; (**H**) The relationship between PA signal intensities and concentrations of Ti_3C_2/TiO_2 in vivo.

from 0 to 200 ppm, the brightness and intensity of the PA signal steadily increased. A direct relationship was observed and depicted in Figure 4F between the concentration of Ti_3C_2/TiO_2 and photoacoustic signal. Based on the aforementioned findings, it is inferred that Ti_3C_2/TiO_2 exhibits commendable photoacoustic properties. Moreover, the in vivo photoacoustic properties of Ti_3C_2/TiO_2 were investigated in Hep3B tumor-bearing mice. Subcutaneous xenograft models were established and Ti_3C_2 was administered through the tail vein. Photoacoustic imaging was observed and recorded. The photoacoustic (PA) signal at the tumor site increased over time, with a maximum of 6 hours after injection (Figure 4G and H). The PA signal significantly decreased 24 hours after injection, indicating the successful accumulation of Ti_3C_2/TiO_2 in the tumor tissue and its potential for long-term treatment. These findings demonstrate the efficient internalization of Ti_3C_2 into HCC cells and its ability to induce a photoacoustic effect on tumor models, supporting its potential for targeted tumor therapy.

The Anticancer Performance in vitro and the Cellular Internalization

Based on the above results analyzing the uptake of Ti_3C_2 in HCC tumors, we investigated its effect on cell viability. Initially, we evaluated the cytotoxicity of Ti_3C_2/TiO_2 in vitro using the CCK-8 assay, where it was incubated with three HCC cell lines including Hep3B, SK-Hep-1, Bel-7402, and normal cell HEK-293T. As indicated in Figure 5A, cell viability remains at 80% of the control even when incubated with high concentrations of Ti_3C_2 (60 μg/mL) for 24 hours, implying that Ti_3C_2 has excellent therapeutic potential due to its low cellular toxicity. The therapeutic effect of Ti_3C_2

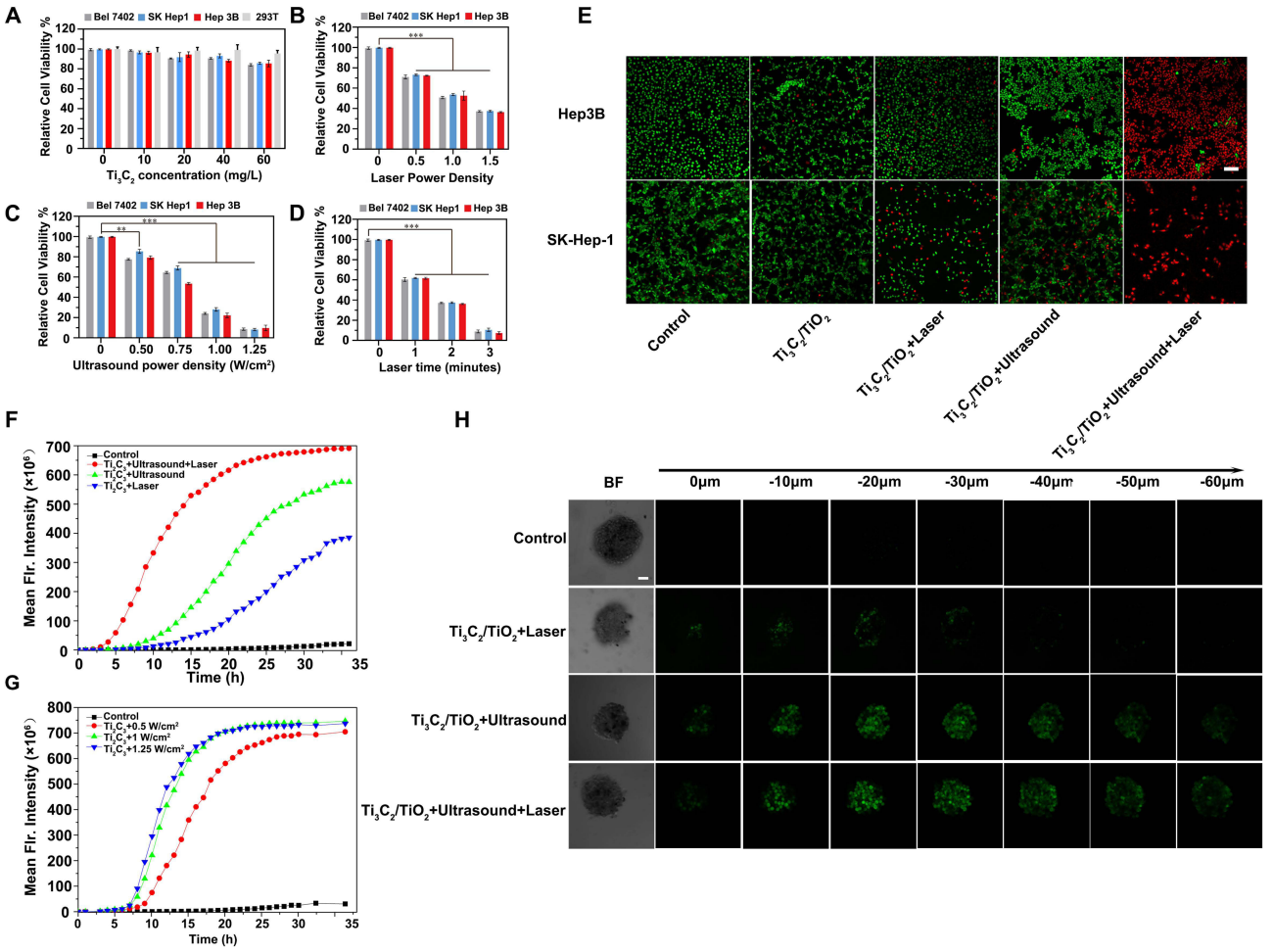

Figure 5 Cell viability analysis in Ti_3C_2/TiO_2 treated HCC cells. (**A**) The viability of Hep3B, Bel-7402, SK-Hep-1 cancer cells as well as HEK 293T cells incubated with different concentrations Ti_3C_2 for 24 h; (**B**) Cell viability of Hep3B, Bel-7402, SK-Hep-1 cells incubated with Ti_3C_2 at various power density after NIR light irradiation (808 nm, 2 min, 20 ppm); (**C**) Cell viability of Hep3B, Bel-7402, SK-Hep-1 cells incubated with Ti_3C_2 at various ultrasonic powers under ultrasonic after 12 h (3 min, 20 ppm); (**D**) Cell viability of Hep3B, Bel-7402, SK-Hep-1 cells incubated with Ti_3C_2 at various irradiation times after NIR light irradiation (808 nm, 1.5 W/ cm^2, 20 ppm); (**E**) Calcein AM (green) and propidium iodide (red) co-staining fluorescence imaging of Hep3B and SK-Hep-1 cells after different treatments. NIR light irradiation (20 ppm, 808 nm, 1 W/cm^2, 5 min) was conducted after cells were incubated with Ti_3C_2. Scale bar: 200 μm; (**F**) The ROS generation of Ti_3C_2 under different treatment in Hep3B cells; (**G**) The ROS generation of Ti_3C_2 under different treatments in Hep3B cells; (**H**) The ROS generation of the tumor mammospheres under different treatment.
Notes: ** indicates $p<0.01$, ***indicates $p<0.005$ between groups.

/TiO_2 induced by laser and ultrasound was evaluated. Cancer cell viability decreased as the laser power density increased under laser irradiation. Cell viability dropped below 40% when the laser power density reached 1.5 W/cm^2 (Figure 5B). Cell viability significantly decreased as ultrasound power increased in all three cell lines, as demonstrated in Figure 5C. At the highest ultrasound power intensity (1.25 W/cm^2), only about 10% of cells remained viable. Longer laser irradiation treatments resulted in more cancer cell death, as displayed in Figure 5D. Furthermore, both laser and ultrasound treatment caused concentration- or time-dependent cell death in Hep3B cells (Figure S2). Importantly, the in vitro anticancer performance of Ti_3C_2 was systematically investigated using Calcein AM/PI detected by confocal laser scanning microscopy (CLSM) as shown in Figure 5E. Further, ultrasound and near-infrared (NIR) laser treatments of Ti_3C_2 resulted in the highest rate of dead cells labeled by red staining, demonstrating the best antitumor effect induced by synergistic photothermal and sonodynamic therapies.

ROS Was Involved in Ti_3C_2/TiO_2-Induced Photothermal and Sonodynamic Therapy

ROS has been identified as a crucial molecular trigger for sonodynamic therapy. We examined the ROS levels following treatment of Ti_3C_2 with synergistic ultrasound and laser. To dynamically monitor the ROS increase, we incubated Hep3B

cells with 2.7-dichlorofluorescein diacetate (DCFH-DA) probes. ROS levels were monitored in real-time using the Incucyte S3 system. As illustrated in Figure 5F, the fluorescence intensity of DCF increased steadily from 5 hours of ultrasound exposure to 35 hours. The Ti_3C_2/TiO_2-induced ROS generation via sonodynamic therapy was significantly higher under ultrasound compared to laser activation. Additionally, the ROS generation of Ti_3C_2 increased proportionally with the ultrasound power. Below 1 W/cm^2 of ultrasound power, the ROS generation of Ti_3C_2/TiO_2 reached its peak (Figure 5G). Importantly, we investigated the level of ROS in three-dimensional mammosphere models that recapitulate the stemness and microenvironment of the original tumor. As demonstrated in Figure 5H, the groups treated with laser irradiation and ultrasound show the strongest green fluorescent signal, covering the entire tumor mammospheres formed by Hep3B. Additionally, a comparable pattern of green signal is observed in the mammospheres treated with ultrasound. However, laser irradiation alone induced a low green signal in the mammospheres, suggesting the exceptional ROS enhancement of the Ti_3C_2/TiO_2 heterostructure induced by ultrasound. A similar ROS alteration was observed in the three-dimensional mammospheres constituted by SK-Hep-1 cells (Figure S3). These findings support the notion that Ti_3C_2 can act as a proficient sonosensitizer, resulting in excellent ROS production for SDT, which is vital for its antitumor efficacy.

Ti_3C_2 Inhibited Tumor Growth in Xenograft Models

To examine the synergistic effect of Ti_3C_2/TiO_2 photothermal and sonodynamic therapy on tumor ablation in vivo, we administered Ti_3C_2-induced SDT and PTT treatment to tumor models. Subcutaneous H22 cells were inoculated in Balb/c mice which were then divided into five groups. The mice were treated with either PBS or Ti_3C_2, and ultrasound and laser treatment modalities were applied as depicted in Figure 6A. The tumors were treated at four-day intervals and observed for 21 days. The tumor volume for each group was recorded and graphed against the treatment intervals. The group treated with laser plus ultrasound had significantly smaller tumors than other groups, indicating a synergistic effect of photothermal and sonodynamic therapy (Figure 6B). Body weight slightly increased in all groups instead of decreasing, showing no obvious toxic effect of photothermal and sonodynamic therapy in vivo (Figure 6C). Finally, all mice were sacrificed, and tumors were harvested. Representative tumor images from each group were displayed in Figure 6D. Tumor growth was inhibited after ultrasound or laser treatment alone, while tumors treated with both ultrasound and laser were the most inhibited. Figure 6E displays the tumor weights from each group, demonstrating that the combined strategy of photothermal and sonodynamic treatment is the most effective in inhibiting tumor growth. All of these outcomes demonstrate that the use of Ti_3C_2/TiO_2-enhanced sonodynamic therapy increases the inhibitory impact on tumor growth, implying significant potential for the combined therapy of photothermal and sonodynamic effects.

Furthermore, hearts, livers, spleens, kidneys, and lungs were collected from each group after 21 days. The H&E staining results revealed no discernible damage or toxic effects. It was demonstrated that Ti_3C_2/TiO_2 and its associated therapies do not have any evident side effects in vivo (Figure 6F). Notably, no noteworthy changes in parameters, such as WBC, NEUT, LYM, RBC, LHGB, HCT, or PLT, were observed in routine blood tests (Figure 6G). Furthermore, liver and kidney function tests did not show significant damage to these organs after treatment with Ti_3C_2 and its associated ultrasound and laser treatment (Figure 6H). ICP results demonstrate that the accumulation of Ti_3C_2/TiO_2 mostly occurs in the liver, suggesting that it is predominantly metabolized by this organ (see Figure 6I). These findings suggest strong blood biocompatibility of Ti_3C_2/TiO_2 in vivo Figure 6I.

Ti_3C_2/TiO_2 Perturbs Oxidative Homeostasis and is Associated with Apoptosis in HCC Tumor

We confirmed the impact of Ti_3C_2-based SDT therapies on HCC cell viability and ROS levels. These results prompted an investigation into the relationship between Ti_3C_2/TiO_2-regulated signaling pathways and cell death. We executed a series of experiments to unravel the molecular mechanisms underlying this effect. Initially, we treated Hep3B or SK-Hep-1 cells with or without laser irradiation and ultrasound treatment. Total RNA lysates were prepared and subjected to RNA-seq analysis. Differences in gene expression between the control and PTT/SDT groups were depicted via volcano plots (Figure 7A and B). Genes that exhibited differential expression in both cell lines post-treatment were identified and counted. The expression of

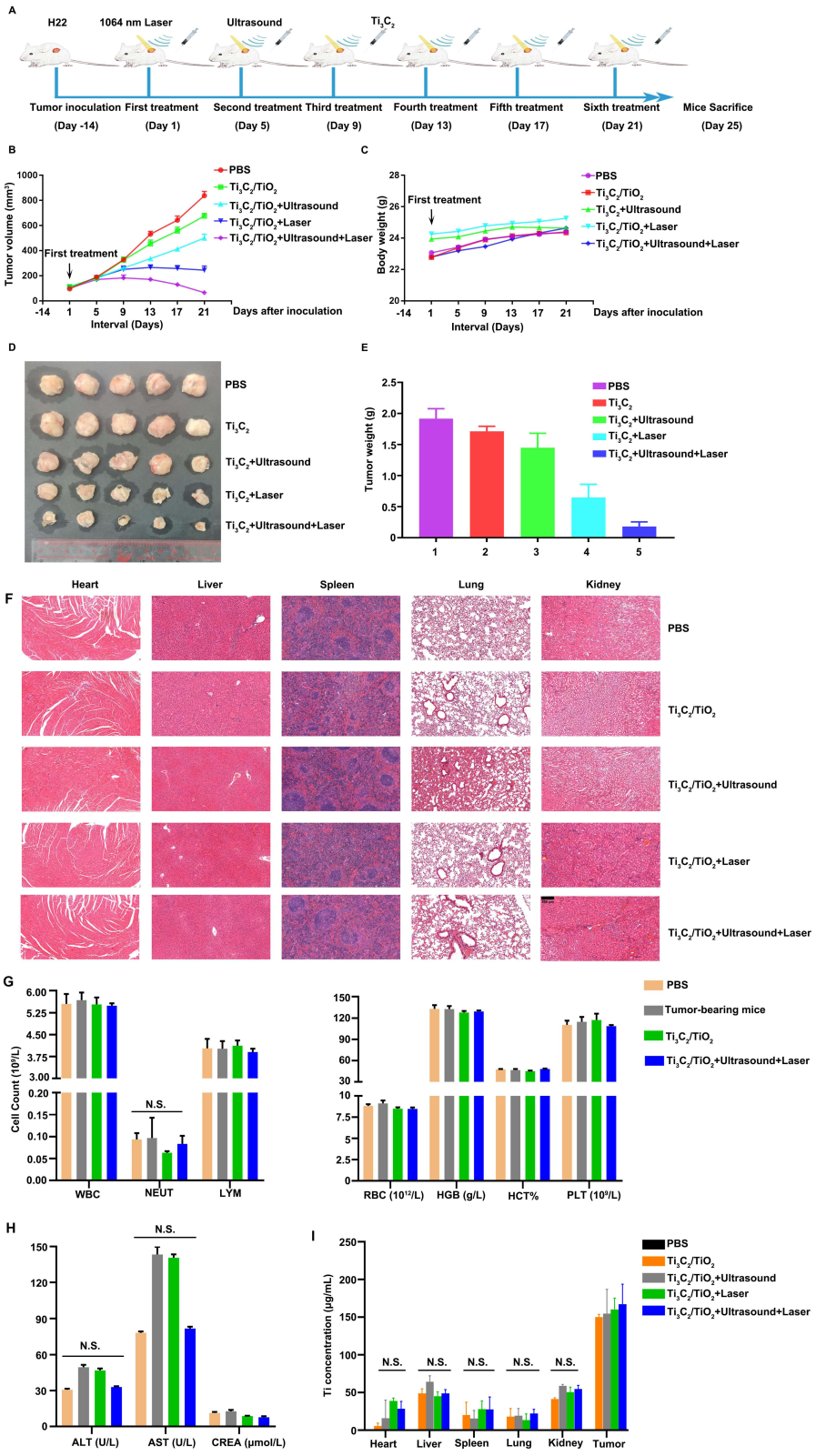

Figure 6 Analysis of tumor-inhibition elicited by Ti_3C_2/TiO_2. (**A**) The scheme depicts the in vivo experiment; (**B**) Tumors size from the indicated groups were recorded and graphed; (**C**) Body weight of each mouse were recorded at the indicated time periods and graphed. (**D**) Tumors were harvested after sacrifice at treatment for 25 days. (**E**) Weight of tumors obtained from each group and graphed. (**F**) H&E staining of indicated tissues from each group; (**G**) Routine blood tests were performed on peripheral blood from indicated groups. White blood cells, neutrophils, lymphocytes, and red blood cells were counted and graphed; (**H**) Alanine transaminase (ALT), Aspartate Transaminase (AST), and creatinine (CREA) levels in peripheral blood were investigated and graphed; I. The concentration of Ti in organs and tumor tissues was measured by an Inductive Coupled Plasma Emission Spectrometer (ICP).

https://doi.org/10.2147/IJN.S457112 DovePress

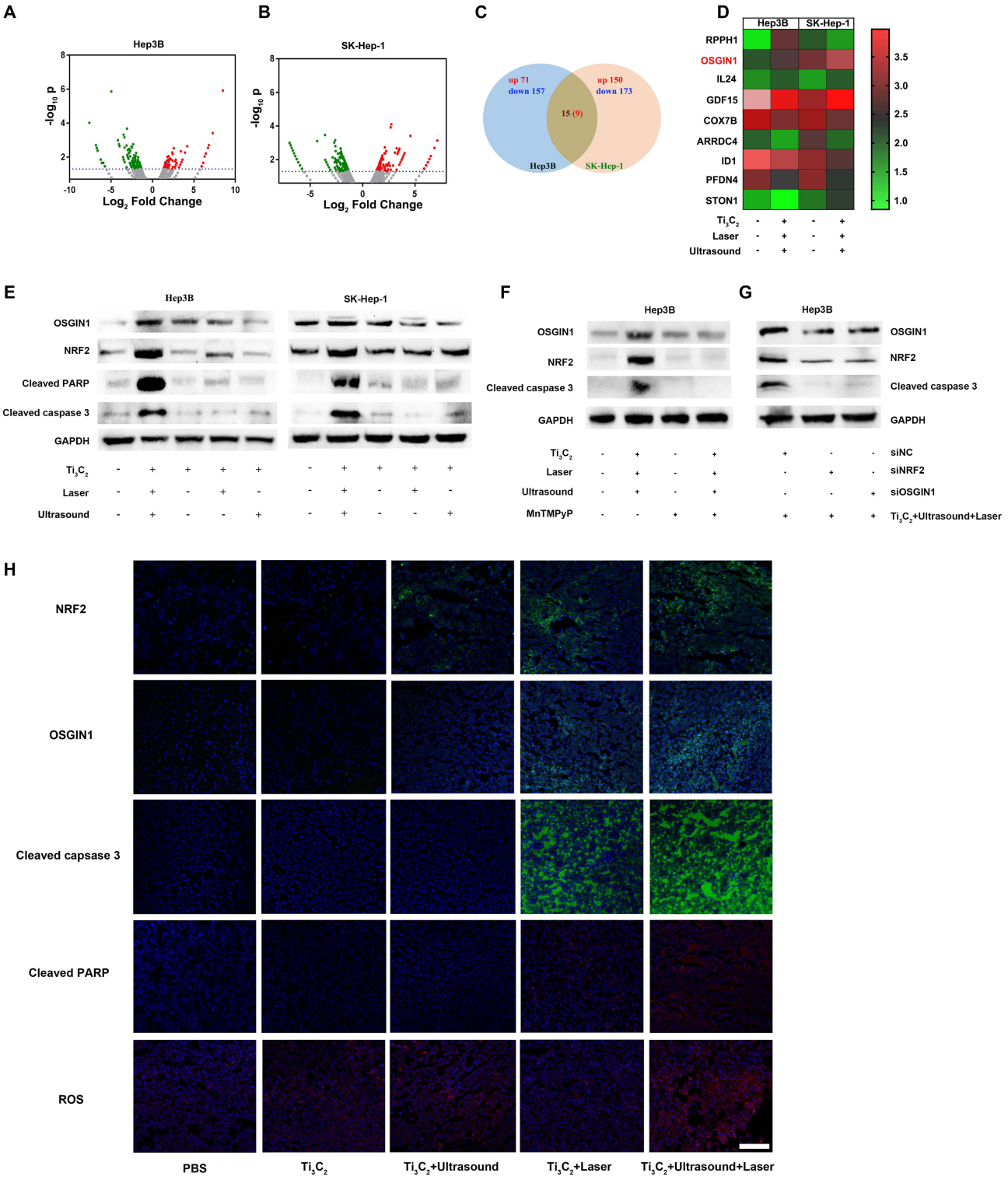

Figure 7 Involvement of OSGIN1-mediated apoptosis in Ti_3C_2/TiO_2 treated HCC cells. (**A**) Volcano map formed from differentially expressed genes after treatment by Ti_3C_2/TiO_2 in Hep3B cells; (**B**) Volcano map formed from differentially expressed genes after treatment by Ti_3C_2/TiO_2 in SK-Hep1 cells; (**C**) Venn gram describing the upregulated and downregulated genes in Hep3B and SK-Hep-1 cells after treatment by Ti_3C_2/TiO_2; (**D**) Expression of 9 upregulated genes in both Hep3B and SK-Hep-1 cells after treatment by Ti_3C_2/TiO_2 were shown in Heatmap; (**E**) Expression of OSGIN1, NRF2, cleaved PARP and cleaved caspase 3 in Hep3B and SK-Hep-1 cells after indicated treatment were investigated by western blot. GAPDH was used as an internal loading control; (**F**) Expression of OSGIN1, NRF2, and cleaved caspase 3 in Hep3B and SK-Hep-1 cells after ROS depletion by MnTMPyP along with indicated treatment were investigated by western blot. GAPDH was used as an internal loading control. (**H**) Expression of NRF2, OSGIN1, cleaved caspase 3 and cleaved PARP were investigated by immunofluorescence assays. Green signals show the expression of indicated protein, while red signals represent ROS levels in different tissues. Nuclei were counterstained with DAPI solution shown as blue signals. Scale bar: 50 μm.

228 or 332 genes significantly changed after treatment in Hep3B or SK-Hep-1 cells, respectively, as evinced by the Venn diagram (Figure 7C). To eliminate the distinction between the cell lines treated with sonodynamic therapy, we selected 15 co-differentially expressed genes in both cell lines. Among them, nine genes exhibited a consistently up-regulated pattern. The up-regulated expression pattern of these nine genes is presented as a heat map in Figure 7D. Upon analyzing these genes, we identified a potential correlation between oxidative stress-induced growth inhibitor 1 (OSGIN1) and ROS. OSGIN1, also known as OKL38, encodes a protein that responds to oxidative stress and regulates cell death.[30] This prompted us to further investigate the relationship between OSGIN1 and SDT after Ti_3C_2/TiO_2 treatment. We examined the expression of genes related to apoptosis following Ti_3C_2/TiO_2 treatment in the presence of laser or ultrasound treatment. We observed that sonodynamic plus photothermal therapy induced by Ti_3C_2/TiO_2 led to the expression of cleaved caspase 3 and cleaved PARP, indicating apoptosis of HCC cells. OSGIN1 and its upstream regulator NRF2 also increased in the SDT-treated group (Figure 7E). To clarify the role of ROS in apoptosis of HCC cells induced by combinatorial therapies, we pre-treated cells with Manganese (III) Tetrakis (1-Methyl-4-Pyridyl) Porphyrin (MnTmPyP), a superoxidase mimic, to eliminate ROS in the case of Ti_3C_2/TiO_2 treatment with laser and ultrasound. Figure 7F clearly shows that the elimination of ROS reversed the increase in OSGIN1 expression. The expression of cleaved caspase 3 and cleaved PARP was reversed upon scavenging ROS via MnTmPyP treatment. Correspondingly, silencing OSGIN1 and NRF2 abolished the expression of cleaved caspase 3 and cleaved PARP. This demonstrates that ROS-modulated OSGIN1 signaling is necessary for SDT-induced apoptosis mediated by Ti_3C_2 (Figure 7G). Taken together, these results demonstrate that OSGIN1 signaling regulated by ROS, played a critical role in the apoptosis of HCC cells induced by Ti_3C_2/TiO_2-mediated sonodynamic and photothermal combination therapies.

Finally, our conclusion was validated on xenograft animal models. Treatment with Ti_3C_2/TiO_2 in combination with ultrasound and laser therapy resulted in a significant increase of ROS in tumor tissues from xenograft mouse models. (bottom panel of Figure 7H). Furthermore, OSGIN1 and its upstream regulator NRF2 were upregulated in the SDT and PTT treated groups (upper panel of Figure 7H). Ti_3C_2/TiO_2-induced photothermal and sonodynamic therapies were found to induce apoptosis in tumor tissues, indicated by the strongest staining of cleaved caspase 3 and PARP in comparison to PBS and other groups (middle panel of Figure 7H). The results obtained from in vitro cell lines are in accordance with in vivo findings, further supporting the conclusion that ROS-modulated OSGIN1 signaling plays a critical role in Ti_3C_2/TiO_2-induced tumor inhibition in both HCC cells and mouse models.

Synergistic Therapy Induced an Immune-Active TME

ROS are reported to be involved in various aspects of immune modulation, including T-cell activation, inflammation, and antigen presentation in the hypoxic tumor microenvironment.[31] It was crucial to reveal the molecular mechanisms by elucidating the role of Ti_3C_2/TiO_2-induced ROS in the immune milieu.[30] The tumor microenvironment (TME), known to have immune-suppressive properties, is linked to the recurrence and deterioration of malignant cancers.[32] Reversing immunosuppression has gained attention for improving the efficacy of tumor ablation.[33,34] Our RNA-seq results (Figure 7D) also demonstrate the modulation of inflammation-associated molecules IL24 by Ti_3C_2/TiO_2 treatment. We are currently investigating the anti-tumor immune response of synergistic therapy for HCC treatment. Following treatment with various therapies, spleen and blood lymphocytes were collected from mice and analyzed via flow cytometry. It is noteworthy that the spleen's $CD8^+$ T cell percentage significantly increased in the group receiving synergistic therapy compared to untreated mice (PBS group) (21.5% versus 13.0%). Interestingly, the synergistic group exhibited stronger activation phenotypes and greater TNF-α production (21.5% versus 6.02%) in splenic $CD8^+$ T cells when compared to other groups. Notably, TNF-α and IFN-γ in $CD4^+$ T cells were also increased, elevating from 4.06% to 14.4% and 1.49% to 4.78%, respectively (refer to Figure 8A). Significant enhancement of T cells anti-tumor activity in the blood of the synergistic group was noted. Consistently, TNF-α levels were increased in both $CD8^+$ and $CD4^+$ T cells (from 7.02% to 19.4% and 5.09% to 9.95%, respectively) while IFN-γ levels were increased in $CD4^+$ T cells (from 6.43% to 24.7%) in the group treated with both laser and ultrasound, compared with other groups (Figure 8B).

Additionally, an increase of $CD4^+$ and $CD8^+$ T cells in tumor tissues was observed through immunohistochemical staining. The production of functional cytokines, such as IFN-γ by $CD8^+$ T cells, was elevated in tumor tissues following Ti_3C_2/TiO_2 activation using laser and ultrasound (Figure S6). Importantly, investigation of immune-modulatory effect of Ti_3C_2 on tumor growth and tumor-draining lymph nodes were investigated in bilateral tumor models. As shown in Figure S7A and B, Ti_3C_2

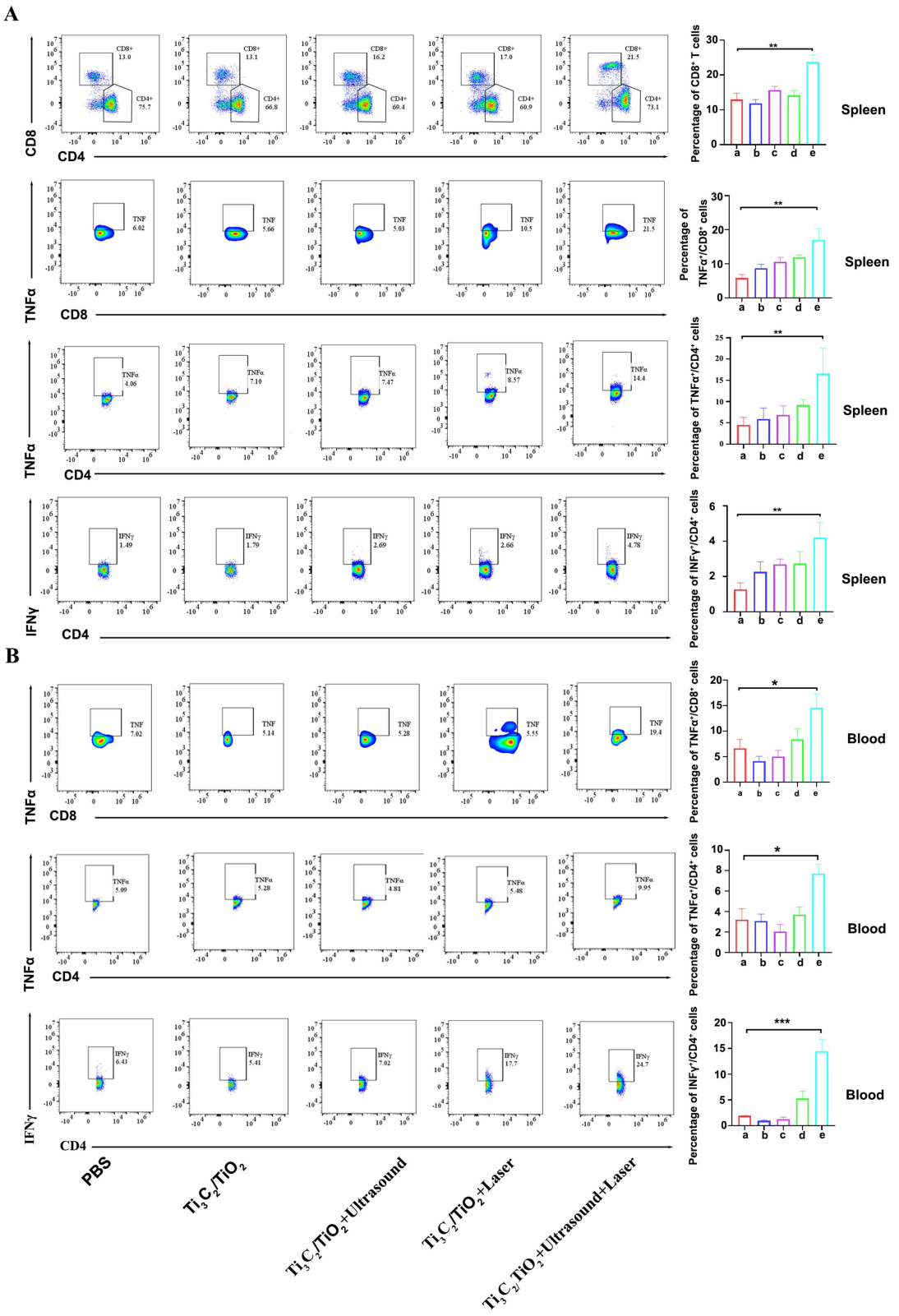

Figure 8 Immune infiltration was analyzed after Ti_3C_2/TiO_2 treatment. (**A**) Spleens from each group (**a**). PBS, (**b**). Ti_3C_2/TiO_2, (**c**). Ti_3C_2/TiO_2+Ultrasound, (**d**). Ti_3C_2/TiO_2 +Laser, (**e**). Ti_3C_2/TiO_2+Ultrasound+Laser. were harvested. Single cell solution was prepared and subjected to flow cytometry assays. $CD8^+/CD4^+$ cells (upper panel), $CD8^+/TNF\alpha^+$, $CD4^+/TNF\alpha^+$cells (midddle panel) and $CD4^+$/ IFN-γ^+ cells (lower panel) were detected and quantification was analyzed as a bar graph; (**B**) $CD8^+/TNF\alpha^+$ cells were analyzed by flow cytometry and quantification were plotted (upper panel). $CD4^+/TNF\alpha^+$ were analyzed by flow cytometry and quantification was plotted (middle panel). $CD4^+$/ IFN-γ^+ cells were analyzed by flow cytometry and quantification was plotted (lower panel).

Notes: * indicates $p<0.05$, **indicates $p<0.01$, *** indicates $p<0.005$ between groups respectively, which means statistical significance.

/TiO_2 treatment along with laser and ultrasound elicited dendritic cell maturation reflected by an increase of $CD80^+$/$CD86^+$ cells implicating activation of the immune system in tumor-draining lymph nodes. This modulatory effect of tumor immune microenvironment elicited by sonodynamic and photothermal therapy of proximal tumor might cause suppression of tumor growth of distal tumor growth (Figure S7D and E). Consistently, P53 as pivotal upstream regulator of NRF2/OSGIN1 signaling, was found to be upregulated after Ti_3C_2/TiO_2 treatment plus ultrasound and laser (Figure S7C). These findings suggest that Ti_3C_2 can transform the immune microenvironment from "immunosuppressive" to "antitumor" and enhance tumor elimination by activating adaptive antitumor immunity.

Conclusions

Ti_3C_2 was successfully synthesized and characterized in the study. It exhibits multi-enzyme activity, such as intrinsic peroxidase (POD) activities that react with H_2O_2 in the tumor microenvironment, constructing a Ti_3C_2/TiO_2 heterostructure in vivo. This integrates photothermal and sonodynamic effects for image-guided cancer therapy and induces multifaceted anticancer immune responses. We observed an ultrasound-induced surge of ROS in Ti_3C_2/TiO_2-treated HCC cells and tumor tissues resulting from sonodynamic therapy. In HCC cells and animal models, we observed synergistic effects of the photothermal and sonodynamic effects of Ti_3C_2/TiO_2. Notably, Ti_3C_2/TiO_2 induced immune-mediated destruction of tumor tissues through recruitment of $CD4^+$ and $CD8^+$ T cells and cytokine secretion, complementing the conventional apoptosis-inducing effect of photothermal and sonodynamic therapies. Our study presents a new approach for ablating HCC tumors using Ti_3C_2/TiO_2 to regulate the tumor microenvironment. This is done by adjusting the ROS balance through the NRF2/OSGIN1 pathway and promoting immune activation. Major findings in different treatments by Ti_3C_2/TiO_2 were summarized in Table S1.

Data Sharing Statement

All the data supporting this study are available from the corresponding authors upon reasonable request.

Ethical Approval Statement

All animal experiments were approved by the Animal Ethics Committee of the Fifth Affiliated Hospital, Sun Yat-sen University. Detailed information can be found in the "Materials and Methods" Section.

Author Contributions

All authors made a significant contribution to the work reported, whether that is in the conception, study design, execution, acquisition of data, analysis, and interpretation, or in all these areas; took part in drafting, revising or critically reviewing the article; gave final approval of the version to be published; have agreed on the journal to which the article has been submitted; and agree to be accountable for all aspects of the work.

Funding

This work was supported by the Guangdong Basic and Applied Basic Research Foundation (2023A1515010620, 2022A1515012482), Youth Program of National Natural Science Foundation of China 82001837, Zhuhai basic and applied basic research project ZH22017003210009PWC, Excellent Young Researchers Program of the 5th Affiliated Hospital of SYSU WYYXQN-2021010, and the Guangdong-Hong Kong-Macao University Joint Laboratory of Interventional Medicine Foundation of Guangdong Province (2023LSYS001).

Disclosure

Hailing Yu, Yongquan Huang and Zhisheng Nong are co-first authors for this study. The authors declare no conflicts of interest in this work.

References

1. Siegel RL, Miller KD, Fuchs HE, Jemal A. Cancer statistics, 2022, CA. *Cancer J Clin*. 2022;72:7–33. doi:10.3322/caac.21708
2. Villanueva A, Longo DL, Longo DL. Hepatocellular Carcinoma. *N Engl J Med*. 2019;380:1450–1462. doi:10.1056/NEJMra1713263

3. Miller KD, Nogueira L, Devasia T, et al. Cancer treatment and survivorship statistics, 2022, CA. *Cancer J Clin*. 2022;72:409–436. doi:10.3322/caac.21731
4. Kadkhoda J, Tarighatnia A, Barar J, Aghanejad A, Davaran S. Recent advances and trends in nanoparticles based photothermal and photodynamic therapy. *Photodiagn Photodyn Ther*. 2022;37:102697. doi:10.1016/j.pdpdt.2021.102697
5. Zhu L, Li Y, Jiang M, et al. Self-assembly of precisely fluorinated albumin for dual imaging-guided synergistic chemo–photothermal–photodynamic cancer therapy. *ACS Appl Mater Inter*. 2023;15:2665–2678—.
6. Wang X, Wang C, Xu Y, et al. The multifunctional Prussian blue/graphitic carbon nitride nanocomposites for fluorescence imaging-guided photothermal and photodynamic combination therapy. *RSC Adv*. 2023;13:335–343. doi:10.1039/D2RA07022G
7. Deng X, Shao Z, Zhao Y. Solutions to the drawbacks of photothermal and photodynamic cancer therapy. *Adv. Sci*. 2021;8. doi:10.1002/advs.202002504
8. Hu H, Feng W, Qian X, Yu L, Chen Y, Li Y. Emerging nanomedicine-enabled/enhanced nanodynamic therapies beyond traditional photodynamics. *Adv Mater*. 2021;33. doi:10.1002/adma.202005062
9. Fan Z, Zhuang C, Wang S, Zhang Y. Photodynamic and photothermal therapy of hepatocellular carcinoma. *Front Oncol*. 2021;11. doi:10.3389/fonc.2021.787780
10. Xu K, Chang M, Wang Z, et al. Multienzyme-mimicking lacoo 3 nanotrigger for programming cancer-cell pyroptosis. *Adv Mater*. 2023;35:e2302961. doi:10.1002/adma.202302961
11. Yu H, Tang K, Cai Z, et al. Carbon Dots-Based Nanozyme for Drug-Resistant Lung Cancer Therapy by Encapsulated Doxorubicin/siRNA Cocktail. *Int J Nanomed*. 2023;18:933–948. doi:10.2147/IJN.S390984
12. Chen J, Fu W, Jiang F-L, Liu Y, Jiang P. Recent advances in 2D metal carbides and nitrides (MXenes): synthesis and biological application. *J Mat Chem B*. 2023;11:702–715—.
13. Du W, Chen J, Wang L, et al. Oxygen-deficient titanium dioxide-loaded black phosphorus nanosheets for synergistic photothermal and sonodynamic cancer therapy. *Biomater Adv*. 2022;136:212794. doi:10.1016/j.bioadv.2022.212794
14. Um W, K PKE, Lee J, Kim CH, You DG, Park JH. Recent advances in nanomaterial-based augmented sonodynamic therapy of cancer. *Chem Commun*. 2021;57:2854–2866. doi:10.1039/D0CC07750J
15. Lafond M, Yoshizawa S, Umemura S-I. Umemura, Sonodynamic Therapy: Advances and challenges in clinical translation. *J Ultrasound Med*. 2019;38:567–580. doi:10.1002/jum.14733
16. Li Y, Yang J, Sun X. Reactive oxygen species-based nanomaterials for cancer therapy. *Front Chem*. 2021;9:650587
17. Wu M, Ding Y, Li L. Recent progress in the augmentation of reactive species with nanoplatforms for cancer therapy. *Nanoscale*. 2019;11:19658–19683. doi:10.1039/C9NR06651A
18. Guo J, Pan X, Wang C, Liu H. Molecular Imaging-Guided Sonodynamic Therapy. *Bioconjugate Chem*. 2021;33:993–1010. doi:10.1021/acs.bioconjchem.1c00288
19. Sun L, Wang P, Zhang J, et al. Design and application of inorganic nanoparticles for sonodynamic cancer therapy. *Bio Sci*. 2021;9:1945–1960. doi:10.1039/D0BM01875A
20. Son S, Kim JH, Wang X, et al. Multifunctional sonosensitizers in sonodynamic cancer therapy. *Chem Soc Rev*. 2020;49:3244–3261. doi:10.1039/C9CS00648F
21. Wang C, Tian Y, Wu B, Cheng W. Recent progress toward imaging application of multifunction sonosensitizers in sonodynamic therapy. *Int j Nanomed*. 2022;17:3511–3529. doi:10.2147/IJN.S370767
22. Balou S, Shandilya P, Priye A. Carbon dots for photothermal applications. *Front Chem*. 2022;10. doi:10.3389/fchem.2022.1023602
23. Xiao Y, Pandey K, Nicolás-Boluda A, et al. Synergic Thermo- and pH-sensitive hybrid microgels loaded with fluorescent dyes and ultrasmall gold nanoparticles for photoacoustic imaging and photothermal therapy. *ACS Appl Mater Inter*. 2022;14:54439–54457. doi:10.1021/acsami.2c12796
24. Paściak A, Marin R, Abiven L, et al. Quantitative Comparison of the Light-to-Heat Conversion Efficiency in Nanomaterials Suitable for Photothermal Therapy. *ACS Appl Mater Inter*. 2022;14:33555–33566. doi:10.1021/acsami.2c08013
25. Zhang L, Yang A, Ruan C, et al. Copper-Nitrogen-Coordinated Carbon Dots: transformable Phototheranostics from Precise PTT/PDT to Post-Treatment Imaging-Guided PDT for Residual Tumor Cells. *ACS Appl Mater Inter*. 2023;15:3253–3265—.
26. Ge EJ, Bush AI, Casini A, et al. Connecting copper and cancer: from transition metal signalling to metalloplasia. *Nat Rev Cancer*. 2022;22:102–113. doi:10.1038/s41568-021-00417-2
27. Yue Q, Sun J, Chen S, et al. Hierarchical Mesoporous MXene–NiCoP Electrocatalyst for Water-Splitting. *ACS Appl Mater Inter*. 2020;12:18570–18577. doi:10.1021/acsami.0c01303
28. Rakhi RB, Ahmed B, Hedhili MN, Anjum DH, Alshareef HN. Effect of Postetch Annealing Gas Composition on the Structural and Electrochemical Properties of Ti2CTx MXene Electrodes for Supercapacitor Applications. *Chem Mater*. 2015;27:5314–5323. doi:10.1021/acs.chemmater.5b01623
29. My Tran N, Thanh Hoai Ta Q, Noh J-S. Unusual synthesis of safflower-shaped TiO2/Ti3C2 heterostructures initiated from two-dimensional Ti3C2 MXene. *Appl Surf Sci*. 2021;538:148023. doi:10.1016/j.apsusc.2020.148023
30. Huang J, Xiao Z, An Y, et al. Nanodrug with dual-sensitivity to tumor microenvironment for immuno-sonodynamic anti-cancer therapy. *Biomaterials*. 2021;269:120636. doi:10.1016/j.biomaterials.2020.120636
31. Zhao C, Deng H, Chen X. Harnessing immune response using reactive oxygen Species-Generating/Eliminating inorganic biomaterials for disease treatment. *Adv Drug Delivery Rev*. 2022;188:114456. doi:10.1016/j.addr.2022.114456
32. Quail DF, Joyce JA. Microenvironmental regulation of tumor progression and metastasis. *Nature Med*. 2013;19:1423–1437. doi:10.1038/nm.3394
33. Kim M, Lee JS, Kim W, et al. Aptamer-conjugated nano-liposome for immunogenic chemotherapy with reversal of immunosuppression. *J Control Rel*. 2022;348:893–910. doi:10.1016/j.jconrel.2022.06.039
34. Yin Y, Jiang T, Hao Y, et al. Cascade catalytic nanoplatform based on ions interference strategy for calcium overload therapy and ferroptosis. *Int J Pharm*. 2021;606:120937. doi:10.1016/j.ijpharm.2021.120937